

Room temperature electrically pumped topological insulator lasers

Jae-Hyuck Choi¹, William E. Hayenga^{1,2}, Yuzhou G. N. Liu¹, Midya Parto², Babak Bahari¹,

Demetrios N. Christodoulides², and Mercedeh Khajavikhan^{1,2*}

¹Ming Hsieh Department of Electrical and Computer Engineering, University of Southern California, Los Angeles, California 90089, USA.

²CREOL, The College of Optics & Photonics, University of Central Florida, Orlando, Florida 32816–2700, USA.

*email: khajavik@usc.edu

Abstract

Topological insulator lasers (TILs) are a recently introduced family of lasing arrays in which phase locking is achieved through synthetic gauge fields. These single frequency light source arrays operate in the spatially extended edge modes of topologically non-trivial optical lattices. Because of the inherent robustness of topological modes against perturbations and defects, such topological insulator lasers tend to demonstrate higher slope efficiencies as compared to their topologically trivial counterparts. So far, magnetic and non-magnetic optically pumped topological laser arrays as well as electrically pumped TILs that are operating at cryogenic temperatures have been demonstrated. Here we present the first room temperature and electrically pumped topological insulator laser. This laser array, using a structure that mimics the quantum spin Hall effect for photons, generates light at telecom wavelengths and exhibits single frequency emission. Our work is expected to lead to further developments in laser science and technology, while opening up new possibilities in topological photonics.

Introduction

In condensed matter physics, topological insulators (TIs) represent a new class of materials with insulating bulks and conducting symmetry-protected surface states¹⁻⁹. The remarkable robustness of these surface currents against local defects and perturbation has led to the application of these materials in quantum transport, spintronic devices, and new transistors, to name a few⁴⁻⁹. While the concept of topological protection was originally conceived for fermionic systems, recent advances have led to designing lattices capable of mimicking analogous responses in the electromagnetic domain¹⁰⁻¹⁹. This is primarily accomplished by realizing artificial gauge fields that emulate the effect of external magnetic fields on light particles through geometric design or modulation. In this respect, photonics has made it possible to study some of the intriguing aspects of topological physics by providing access to synthetic dimensions²⁰⁻²³ and higher order topological insulators²⁴⁻²⁶. Also, photonics allows to study topological behaviors arising due to non-Hermiticity (primarily gain) and nonlinearity that have no immediate counterparts in condensed matter²⁷⁻³³. In return, topological physics has inspired unique light transport schemes that may have important ramifications in integrated photonics³⁴⁻³⁵, quantum optics³⁶⁻³⁷, and laser science³⁸⁻⁵⁰.

Topological insulator lasers (TILs) refer to two-dimensional arrays of emitters that oscillate at the topological edge modes. In photonics, the topological lattice is an artificial structure, designed to generate a synthetic gauge field for photons through direction dependent phase accumulations. The edge modes propagating at the boundary of these lattices feature transport, thus all the active elements at the perimeter of the array are engaged uniformly. The manifestation of this type of mode indicates that the active peripheral entities are phase locked and the system has reached an optimum usage of the pump power⁴⁰. Furthermore, the robustness of the edge

modes to certain classes of perturbations introduces additional benefits by precluding the formation of spurious defect states. These undesired modes tend to compromise the performance of the device by siphoning energy from the main mode. Finally, the additional spectral modes of the cavity can be suppressed by controlling the topological bandgap through adjustment of array parameters. This latter feature is particularly important in semiconductor gain systems with intrinsically broad lineshapes in which single frequency lasing poses a challenge.

So far topological lasing has been demonstrated in optically pumped two-dimensional topological insulator lasers based on active lattices featuring quantum Hall, quantum spin Hall, or valley Hall effect in the absence and presence of external magnetic fields³⁸⁻⁴⁵. In addition, lasing in the edge or zero mode has been achieved in one dimensional SSH arrays, through PT-symmetric⁴⁶⁻⁴⁹ or other selective pumping schemes⁵⁰. Despite the rapid realizations of these optically pumped topological insulator lasers, devices based on electrical injection are still in their infancy. What makes this transition challenging is designing a topological structure that allows for both efficient carrier injection and large mode confinement. To this end, recently, an electrically pumped THz quantum cascade topological insulator laser was demonstrated⁴⁴ in which the edge mode is formed at the boundary of two valley Hall photonic crystals possessing valley Chern numbers of $\pm 1/2$. However, in order to reach lasing, this array was cooled to a cryogenic temperature of 9 K.

Here, we report the first room temperature, electrically pumped topological insulator laser that operates at telecom wavelengths. Our non-magnetic topological insulator array imitates the quantum spin Hall effect for photons through a periodic array of resonators coupled through an aperiodic set of auxiliary link structures. When the resonators at the perimeter of the array are electrically pumped, a uniform and coherent edge mode is excited. We further demonstrate that

the topological property of the system gives rise to single frequency lasing, despite the presence of multiple modes when the array's peripheral elements are locally excited. Our work shows for the first time the feasibility of realizing electrically pumped room temperature topological laser arrays that upon further developments can drive technological needs in related areas.

Results

Design and Fabrication. A schematic of our electrically pumped topological insulator laser is depicted in Fig. 1a. The array is composed of a 10×10 network of microring resonators coupled via a set of anti-resonant link objects, all fabricated on a III-V semiconductor wafer. Figure 1b displays the SEM image of the topological array in an intermediate fabrication stage. The structure implements the quantum spin Hall Hamiltonian for photons by modulating the relative position of the links in each row (see Fig. 1c)^{12,15,40}. In order to promote edge mode lasing, gain is only provided to the peripheral elements through the incorporation of metal electrodes, while the rest of the array is left unpumped to prevent spurious lasing in the bulk. The wafer as shown in Fig. 1d is composed of lattice matched epitaxially grown layers of $\text{In}_x\text{Ga}_{1-x}\text{As}_y\text{P}_{1-y}$ on an undoped InP substrate (see Supplementary Note 1 for details about wafer structure). The design of the wafer structure and the geometry of individual ring resonators are co-optimized in order to efficiently funnel electron and hole carriers into the active region under electrical pumping while at the same time allowing the structure to support a confined optical mode that adequately overlaps with the multiple quantum wells (MQWs). Figure 1e shows the structure of a single resonator at the boundary of the lattice.

To demonstrate lasing by electrical pumping at room temperature, the radii of the ring resonators (R) and their widths (w) are chosen to be $15 \mu\text{m}$ and $1.4 \mu\text{m}$, respectively. The cross

section of the resonators is designed to promote lasing in the fundamental transverse electric mode (TE₀). (see Supplementary Note 2 for details about electromagnetic simulations). The links are of the same widths (w), but their radii of curvature (R_L) are 2.25 μm and the lengths of their straight sections (L_L) are 3 μm . Here the links are intentionally designed with a small radius of curvature in order to prevent their direct contribution through standalone lasing. The gap size between the ring resonators and the off-resonant links (s) is designed to be 200 nm. This allows a frequency splitting of ~ 31 GHz (0.245 nm in wavelength) between two neighboring resonators (see Supplementary Note 3 for deriving the coupling coefficient through measuring frequency splitting). The coupling strength dictates the topological bandgap of the structure, hence effectively determining the longitudinal modal content of the cavity. A stronger coupling also indicates that the edge mode can withstand larger defects, perturbations, and detunings^{12,15,40}. In order to emulate a synthetic gauge field, throughout the array, the position of the links are judiciously vertically shifted from one row to another. Depending on the offset of the link resonators, the photon acquires an asymmetric phase of $\pm 2\pi\alpha$, where α is given as a function of the position shift Δx , such that $\alpha = 2n_{\text{eff}}\Delta x/\lambda$ ^{15,40}. Here α is designed to be 0.25 corresponding to a Δx of 60 nm. For a given Δx , the photonic dynamics are equivalent to having α quanta of synthetic magnetic flux penetrating each plaquette. This results in two topologically nontrivial edge states at the boundary of the lattice^{12,15,40}.

The laser arrays are fabricated on a molecular beam epitaxy (MBE) grown InGaAsP/InP semiconductor wafer by using several stages of lithography and etching, as well as deposition of various materials (metals and dielectrics). The gain region consists of an undoped 10-multiple quantum well film with a thickness of 320 nm, sandwiched between the n - and p -doped InP cladding layers (for details about the wafer structure and fabrication steps see Supplementary Note

1). Considering that the mobility of holes is significantly lower than that of electrons, in our current design, the anode electrodes are positioned directly on top of the cavities, while the cathode electrodes are incorporated at the side of the lattice. Finally, in order to avoid uneven current injection into the large number of edge resonators, we used a set of 12 anode-electrodes (3 on each side of the lattice).

Characterization. We first examine the fabricated electrically pumped structures under optical pumping. To characterize the samples, we use a micro- photoluminescence setup to measure the emission spectrum and observe the intensity profile of the lasers. In order to selectively provide optical gain to the topological edge mode, only the outer perimeter of the lattice is optically pumped using a pulsed laser with a nominal wavelength of 1064 nm (15 ns pulse width and 0.4% duty cycle). The pump is applied from the back of the sample (through the substrate) and the emission spectrum is collected from the same side. A set of intensity masks and a knife edge are used to image the desired pump profile on the sample (The details of the measurement setup can be found in Supplementary Note 4). Figure 2a shows the scattered emission intensity profile of the pumped array. In order to characterize the spectral content of the emitted intensity, we measure the spectrum of the light emitted from the perimeter of the array and the grating output coupler. Figure 2b shows the photoluminescence spectra when the topological cavity is optically pumped at a peak pump intensity of 15.4 kW/cm^2 . A sharp single mode resonance is observed from the peripheral sites as well as the output grating coupler. To further investigate the topological edge mode, the emission spectrum from the output grating was measured as a function of peak pump intensity. As shown in Fig. 2c, the laser remains single moded over a wide range of pump intensities up to $\sim 25 \text{ kW/cm}^2$. Figure 2d shows the light-light curve associated with this device

where the threshold of lasing is 7.84 kW/cm^2 . These results clearly confirm the presence of spectrally single frequency edge modes in this lattice under optical pumping.

Next, we measure the emission properties of the topological laser arrays under electrical pumping. Figure 3a shows a microscope image of the fabricated electrically pumped TIL array used in our study. In this figure, the cathode electrodes (dark orange), vertically separated by a thick layer of benzocyclobutene (BCB), appear in a different color from the anode electrodes (bright orange). A collection of twelve individually controlled anode electrodes ensures that current is uniformly applied to all the edge elements. On the other hand, all cathode branches are connected to each other. To characterize the electroluminescent properties of the topological insulator lasers, a pulsed current driver (ILS Lightwave LDP-3840B) is used (duration: 300 ns, period: 50 μs). The pulsed pumping prevents detuning of the edge elements from the rest of the array due to heating. Figure 3b shows the collected electroluminescence emission profile from the topological insulator laser. The slightly uneven scattering intensity profile is attributed to the inhomogeneities in the structure since the emission is collected from the back of the sample. In our electrically pumped samples, because of the non-uniformities of the BCB layer, the gratings remained unpumped. As a result, here, instead the spectra were measured from the scattered light emanating from the sites located at the perimeter of the lattice. Figure 3c shows the emission spectrum of the device as a function of the injected peak pulsed current. This spectrum was collected from the brightest peripheral site (R3). The plot shows that as the injected current is increased, a sharp single mode lasing peak appears along with a rapid increase in the emitted intensity. It should be noted that the spectra measured at other sites of this lattice exhibit the same emission peak wavelength albeit with different intensities (see Supplementary Note 5). Figure 3d displays the light-current (L-I) curve of this laser, which shows stimulated emission with a

threshold peak current of ~ 500 mA (equivalent to a threshold peak current of ~ 14 mA per ring or a current density of ~ 11 kA/cm²). The electrical characteristic curves (I-V curves) of a three-ring laser (when only one electrode is pumped) and the full TIL are provided in the Supplementary Information (please see Note 6). Further experimental observations confirming that topological lasers outperform trivial lattices in terms of spectral purity, as well as robustness to defects is provided in the Supplementary Information (please see Notes 7 and 8).

Discussion

In order to verify the nature of the lasing mode and study the relationship between the local modes and the topological edge mode, we change our injection pattern by only applying current to one of the twelve electrodes at a given time (see Fig. 4a). We then measure the emission spectrum from the same site. In this case, we supply significantly larger current levels to be able to assess the presence of the localized modes as well as the topological edge mode. We also modify the current pulse width to 100 ns to prevent the laser from being damaged due to overheating. Figure 4b shows the measured spectra when various sets of three-ring-resonators (R3, R2, L5 and R4) are pumped. Their spectral response confirms the presence of various locally excited modes in each site. These local modes can belong to individual rings, caused by small but inevitable defects, or can even be formed because of the pump induced local detunings. While the distribution of the local modes change from one site to another, the topological edge mode at a wavelength of 1503 nm persists in all these measurements (within the grey shaded area), confirming that it is indeed the collective response from the entire array perimeter elements. Clearly, here the interplay between the edge mode and the pump profile ensures the excitation of the topological edge mode even when a few selected rings at the edge are pumped. When all

perimeter elements are coupled to each other, the topological edge mode lases unambiguously while all spurious modes get suppressed. This selective effect that is attributed to the topological nature of modes distinguishes TILs from conventional laser systems. To further confirm that the emission from various sites belongs to an extended topological edge mode, the coherence between various neighboring elements is examined by overlapping their fields and observing the resulting fringes in the image plane (see Supplementary Note 9 for details about coherence measurement). These measurements together with the observed single mode lasing operation can be an indication of a widespread coherence over the entire edge elements in the topological laser array. However, additional interference measurements are needed between edge elements that are further apart in order to fully validate this claim.

In conclusion, our paper reports the first demonstration of room temperature electrically pumped topological insulator lasers, capable of operating at telecommunication wavelengths. Our topological laser structures are composed of coupled ring resonators and links arranged in an aperiodic lattice and emulate the quantum spin Hall Hamiltonians. The fabrication of these TILs on InGaAsP/InP heterostructures involves precise multi-step lithography/etching/deposition/annealing processes. The lasers clearly show single frequency emission and the mode appears to be extended across all the gain elements at the periphery of the lattice. Future works may involve more efficient current injection schemes based on suspended graphene sheets as transparent electrodes⁵¹⁻⁵². Furthermore, the chirality (rotation direction) of the topological edge mode can be unambiguously set by incorporating internal S-bends in the micro-resonators(see Supplementary Note 10)^{40,53,54}. Our work is expected to pave the way towards the realization of a new class of electrically pumped coherent and phase-locked laser arrays that operate at a single frequency and an extended spatial mode. Such lasers, serving as the primary

light source in photonic integrated circuit chips, may have applications in on-chip communications.

Methods

Device fabrication. To fabricate the structures, FOx-16 e-beam resist is spin-coated on a clean piece of wafer and then patterned using high-resolution e-beam lithography followed by development in tetramethylammonium hydroxide (TMAH). The patterns are subsequently transferred into the wafer through a reactive ion etching (RIE) process using H₂:CH₄:Ar (10: 40: 7 sccm) plasma. A 240 nm thick silicon nitride (Si₃N₄) is deposited by plasma-enhanced chemical vapor deposition (PECVD) to ensure insulation and for passivating the side walls. To form the metal electrodes, the cathode-electrode area is defined by photolithography. After sequential dry etching of the Si₃N₄ layer and wet etching of the remaining InP layer, the cathode-electrode is deposited on the InGaAsP *n*-contact layer using Ni/AuGe/Au (5/75/300 nm). An optically transparent polymer (benzocyclobutene, BCB) is then spin-coated on the sample for planarization and for separating cathode- and anode-electrodes at places they overlap. The BCB is etched down using O₂:CF₄ (10: 5 sccm) plasma etching to uncover the top of the ring arrays. The anode-electrodes are defined by photolithography, and then sequential RIE dry-etching and BOE wet-etching processes are performed to remove the Si₃N₄ layer and FOx-16 resist at those places. The anode-electrodes are formed on the InGaAsP *p*-contact layer by thermal evaporation of Ti/Au (15/300 nm) and photoresist liftoff. Finally, a rapid thermal annealing is performed at a temperature of 380 °C for 30 sec and the sample is mounted on a header and wire-bonded for testing. A more detailed description of the fabrication steps can be found in the Supplementary Note 1.

Measurements. The topological insulator lasers were characterized using a micro-electroluminescence (μ -EL) characterization setup. A pulsed current driver (ILS Lightwave LDP-3840B) is used to supply 300 ns (100 ns, in Fig. 4) current pulse for a period of 50 μ s into the topological arrays. Through a set of individual wires connected to each pin of the header, the current is selectively supplied to the desired elements. The light emitted from the back of sample is collected by a 10 \times microscope objective lens with a numerical aperture of 0.26. The emission from the array is then sent to either an NIR camera (Xenics Inc.) or a spectrometer (Princeton Instruments Acton SP2300) with an attached detector array (Princeton Instruments OMA V). For optical pumping characterizations, a 1064 nm pulsed laser (SPI fiber laser, 15 ns pulses with 0.4% duty cycle) is used as a pumping source. A set of amplitude masks and a knife edge are used to shape the pump profile and the desired pump distribution is imaged on the sample. Further details of the characterization setup can be found in Supplementary Note 4.

Data availability

The datasets generated during and/or analysed during the current study are available from the corresponding author on reasonable request.

References

1. Thouless, D. J., Kohmoto, M., Nightingale, M. P. & den Nijs, M. Quantized Hall conductance in a two-dimensional periodic potential. *Phys. Rev. Lett.* **49**, 405–408 (1982).
2. Kane, C. L. & Mele, E. J. Quantum spin Hall effect in graphene. *Phys. Rev. Lett.* **95**, 226801 (2005).
3. Bernevig, B. A. & Zhang, S.-C. Quantum spin Hall effect. *Phys. Rev. Lett.* **96**, 106802 (2006).
4. König, M. et al. Quantum spin Hall insulator state in HgTe quantum wells. *Science* **318**, 766–770 (2007).
5. Hsieh, D. et al. A topological Dirac insulator in a quantum spin Hall phase. *Nature* **452**, 970–974 (2008).
6. Hasan, M. Z. & Kane, C. L. Topological insulators. *Rev. Mod. Phys.* **82**, 3045–3067 (2010).
7. Pesin, D. & MacDonald, A. H. Spintronics and pseudospintronics in graphene and topological insulators. *Nat. Mater.* **11**, 409–416 (2012).
8. Checkelsky, J. G., Ye, J., Onose, Y., Iwasa, Y. & Tokura, Y. Dirac-fermion-mediated ferromagnetism in a topological insulator. *Nat. Phys.* **8**, 729–733 (2012).
9. Qian, X., Liu, J., Fu, L. & Li, J. Quantum spin Hall effect in two-dimensional transition metal dichalcogenides. *Science* **346**, 1344–1347 (2014).
10. Haldane, F. D. M. & Raghu, S. Possible realization of directional optical waveguides in photonic crystals with broken time-reversal symmetry. *Phys. Rev. Lett.* **100**, 013904 (2008).
11. Wang, Z., Chong, Y., Joannopoulos, J. D. & Soljacic, M. Observation of unidirectional backscattering-immune topological electromagnetic states. *Nature* **461**, 772–775 (2009).
12. Hafezi, M., Demler, E. A., Lukin, M. D. & Taylor, J. M. Robust optical delay lines with topological protection. *Nat. Phys.* **7**, 907–912 (2011).

13. Khanikaev, A., Hossein Mousavi, S., Tse, W. et al. Photonic topological insulators. *Nat. Mater.* **12**, 233–239 (2013).
14. Rechtsman, M. C. et al. Strain-induced pseudomagnetic field and photonic Landau levels in dielectric structures. *Nat. Photon.* **7**, 153–158 (2013).
15. Hafezi, M., Mittal, S., Fan, J., Migdall, A. & Taylor, J. M. Imaging topological edge states in silicon photonics. *Nat. Photon.* **7**, 1001–1005 (2013).
16. Chen, W. et al. Experimental realization of photonic topological insulator in a uniaxial metacrystal waveguide. *Nat. Commun.* **5**, 5782 (2014).
17. Wu, L.-H. & Hu, X. Scheme for achieving a topological photonic crystal by using dielectric material. *Phys. Rev. Lett.* **114**, 223901 (2015).
18. Cheng, X. et al. Robust reconfigurable electromagnetic pathways within a photonic topological insulator. *Nat. Mater.* **15**, 542–548 (2016).
19. Kruk, S. et al. Nonlinear light generation in topological nanostructures. *Nat. Nanotechnol.* **14**, 126–130 (2019).
20. Ozawa, T., Price, H. M., Goldman, N., Zilberberg, O. & Carusotto, I. Synthetic dimensions in integrated photonics: from optical isolation to four-dimensional quantum Hall physics. *Phys. Rev. A* **93**, 043827 (2016).
21. Lustig, E. et al. Photonic topological insulator in synthetic dimensions. *Nature* **567**, 356–360 (2019).
22. Dutt, A. et al. A single photonic cavity with two independent physical synthetic dimensions. *Science* **367**, 59–64 (2020).
23. Umucalilar, R. O. & Carusotto, I. Artificial gauge field for photons in coupled cavity arrays. *Phys. Rev. A* **84**, 043804 (2011).

24. Benalcazar, W. A., Bernevig, B. A. & Hughes, T. L. Quantized electric multipole insulators. *Science* **357**, 61–66 (2017).
25. Noh, J. et al. Topological protection of photonic mid-gap defect modes. *Nat. Photon.* **12**, 408–415 (2018).
26. Mittal, S. et al. Photonic quadrupole topological phases. *Nat. Photon* **13**, 692–696 (2019).
27. Hatano, N. & Nelson, D. R. Localization transitions in non-Hermitian quantum mechanics. *Phys. Rev. Lett.* **77**, 570–573 (1996).
28. Lee, T. E. Anomalous Edge State in a Non-Hermitian Lattice. *Phys. Rev. Lett.* **116**, 133903 (2016).
29. El-Ganainy, R. et al. Non-Hermitian physics and PT symmetry. *Nat. Phys.* **14**, 11–19 (2018).
30. Gong, Z. et al. Topological Phases of Non-Hermitian Systems. *Phys. Rev. X* **8**, 031079 (2018).
31. Yao, S. & Wang, Z. Edge states and topological invariants of non-Hermitian systems. *Phys. Rev. Lett.* **121**, 086803 (2018).
32. Parto, M., Liu, Y. G. N., Bahari, B., Khajavikhan, M., & Christodoulides, D. N., Non-Hermitian and topological photonics: optics at an exceptional point. *Nanophotonics* **1** (ahead-of-print)
33. Liu, Y. G. N. et al. Topological Haldane Lattice. In CLEO: QELS_Fundamental Science (pp. FW3A-1). Optical Society of America.
34. He, X. et al. A silicon-on-insulator slab for topological valley transport. *Nat. Commun.* **10**, 872 (2019).
35. Shalaev, M. I. et al. Robust topologically protected transport in photonic crystals at telecommunication wavelengths. *Nat. Nanotechnol.* **14**, 31–34 (2019).

36. Perczel, J. et al. Topological quantum optics in two-dimensional atomic arrays. *Phys. Rev. Lett.* **119**, 023603 (2017).
37. Barik, S. et al. A topological quantum optics interface. *Science* **359**, 666–668 (2018).
38. Bahari, B. et al. Nonreciprocal lasing in topological cavities of arbitrary geometries. *Science* **358**, 636–640 (2017).
39. Harari, G. et al. Topological insulator laser: Theory. *Science* **359**, eear4003 (2018).
40. Bandres, M. A. et al. Topological insulator laser: Experiments. *Science* **359**, eear4005 (2018).
41. Klemmt, S. et al. Exciton-polariton topological insulator. *Nature* **562**, 552–556 (2018).
42. Gong, Y. K. et al. Topological insulator laser using valley-Hall photonic crystals. *ACS Photonics*, **7**, 2089–2097 (2020).
43. Shao, Z. et al. A high-performance topological bulk laser based on band-inversion-induced reflection. *Nat. Nanotechnol.* **15**, 67–72 (2020).
44. Zeng, Y. Q. et al. Electrically pumped topological laser with valley edge modes. *Nature* **578**, 246–250 (2020).
45. Smirnova, D. et al. Room-temperature lasing from nanophotonic topological cavities. *Light Sci Appl* **9**, 127 (2020).
46. Schomerus, H. Topologically protected midgap states in complex photonic lattices. *Opt. Lett.* **38**, 1912–1914 (2013).
47. St-Jean, P. et al. Lasing in topological edge states of a one-dimensional lattice. *Nat. Photon.* **11**, 651–656 (2017).
48. Parto, M. et al. Edge-mode lasing in 1D topological active arrays. *Phys. Rev. Lett.* **120**, 113901 (2018).
49. Ota, Y. et al. Topological photonic crystal nanocavity laser. *Commun. Phys.* **1**, 86 (2018).

50. Zhao, H. et al. Topological hybrid silicon microlasers. *Nat. Commun.* **9**, 981 (2018).
51. Kim, K. et al. Large-scale pattern growth of graphene films for stretchable transparent electrodes. *Nature* **457**, 706–710 (2009).
52. Kim, Y. et al. Graphene-contact electrically driven microdisk lasers. *Nat. Commun.* **3**, 1123 (2012).
53. Ren, J. et al. Unidirectional light emission in PT-symmetric microring lasers. *Opt. Express* **26**, 27153-27160 (2018).
54. Hayenga, W. E. et al. Direct generation of tunable orbital angular momentum beams in microring lasers with broadband exceptional points. *ACS Photonics* **6**, 1895–1901 (2019).

Acknowledgements

We gratefully acknowledge the financial support from DARPA (D18AP00058), Office of Naval Research (N00014-16-1-2640, N00014-18-1-2347, N00014-19-1-2052, N00014-20-1-2522, N00014-20-1-2789), Army Research Office (W911NF-17-1-0481), National Science Foundation (ECCS 1454531, DMR 1420620, ECCS 1757025, CBET 1805200, ECCS 2000538, ECCS 2011171), Air Force Office of Scientific Research (FA9550-14-1-0037, FA9550-20-1-0322), and US–Israel Binational Science Foundation (BSF; 2016381). The authors would like to thank Mordechai Segev from Technion and Patrick Likamwa from CREOL for helpful technical discussions.

Author contributions

J.-H.C., Y.G.N.L. and W.E.H. designed and fabricated the structures. J.-H.C. and Y.G.N.L. performed the experiments. Simulations were carried out by J.-H.C. and M. P. Finally, J.-H.C.,

W.E.H., Y.G.N.L., M. P., B. B., D. N. C. and M. K. discussed the results and contributed in preparing the manuscript.

Additional information

Supplementary Information accompanies this paper at <http://www.nature.com/naturecommunications>

Competing interests: The authors declare no competing interests.

Reprints and permission information is available online at <http://npg.nature.com/reprintsandpermissions/>

Figure Legends

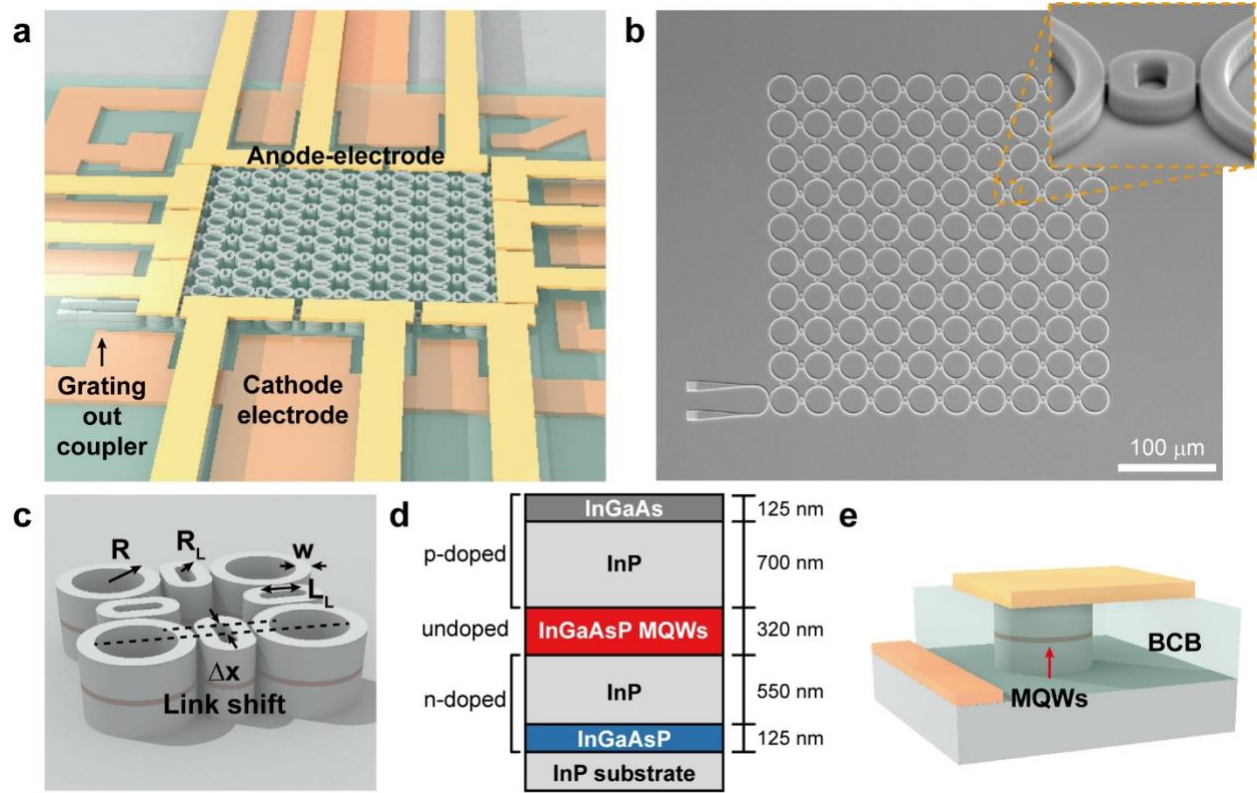


Figure 1 | Electrically pumped topological insulator laser structure. **a** A schematic illustration of an electrically pumped topological insulator laser lattice comprising of a 10×10 network of microring cavities that are coupled to each other through link resonators. **b** Scanning electron microscopy (SEM) image of a fabricated topological insulator laser array. Scale bar is 100 μm . **c** A plaquette consisting of four site microrings and four links. **d** A schematic of the epitaxially grown InGaAsP/InP heterostructure wafer structure shows the location of gain region in the resonators. **e** The position of anode and cathode electrodes with respect to the resonators.

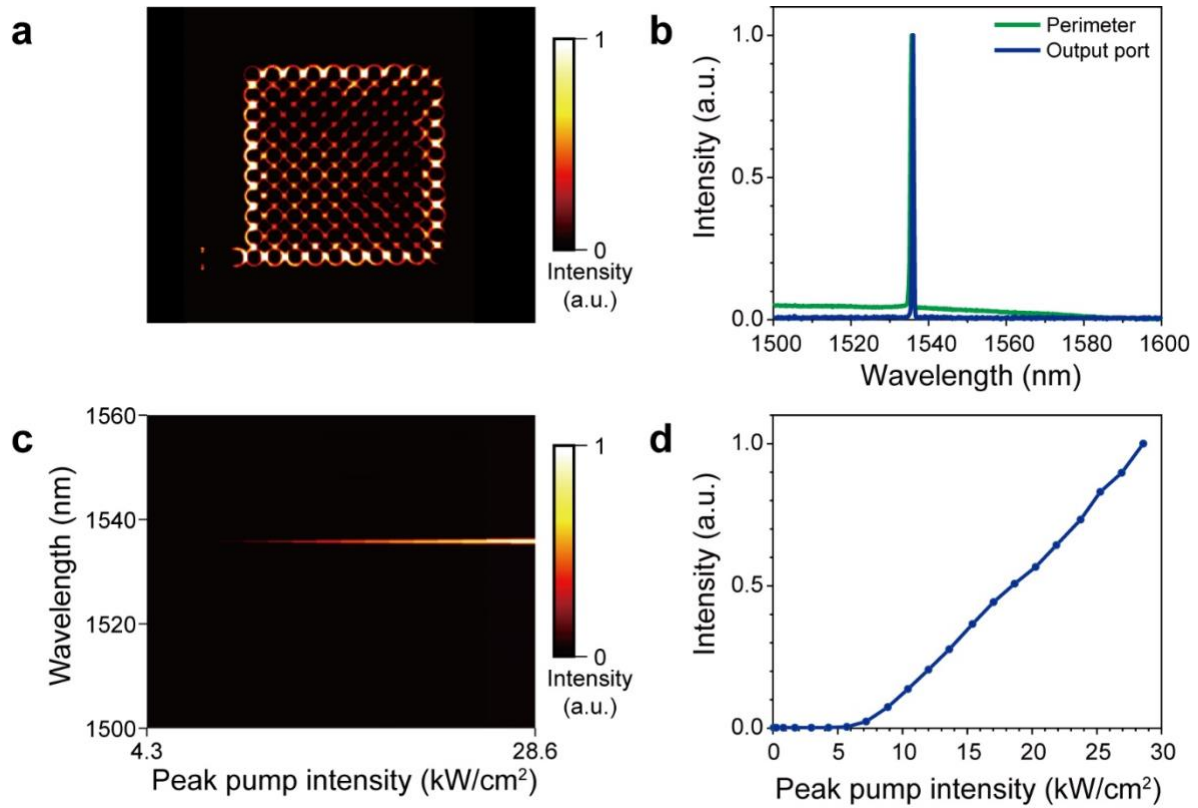


Figure 2 | Topological edge mode lasing under optical pumping. **a** Photoluminescence image from the topological laser array when only its perimeter is pumped. **b** Emission spectra from the grating output coupler and a site on the perimeter at a pump intensity of 15.4 kW/cm^2 . **c** Evolution of the spectrum as a function of the peak pump intensity. The single mode emission with the narrow linewidth is attributed to the topological edge mode. a.u., arbitrary units. **d** Measured output intensity as a function of the peak pump power. The data presented in (c) and (d) were collected from the output port (grating).

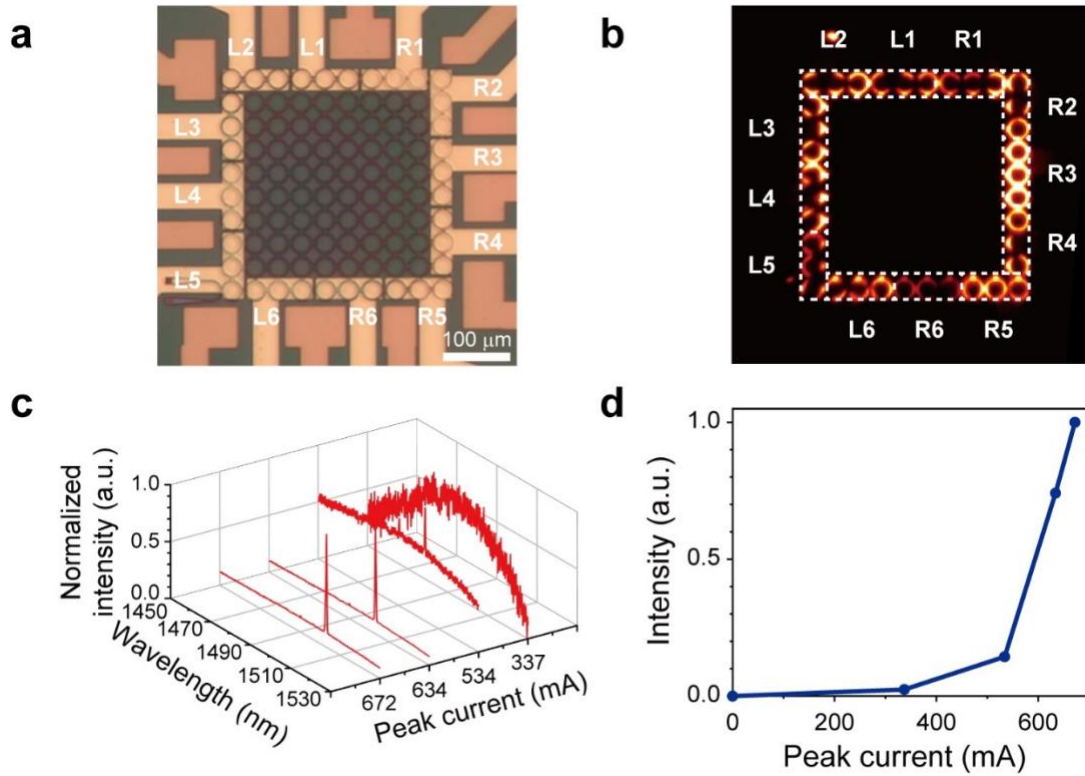


Figure 3 | Electroluminescence measurements of the topological insulator laser. **a** The microscope image of the fabricated topological insulator laser array (top view). In order to selectively excite the topological edge mode, electrodes are designed only at the perimeter of the array (dark orange: cathode, bright orange: anode). R and L labels indicate that the position of the metal pad connected to the electrode is on the right and left, respectively. Scale bar is 100 μm . **b** Intensity profile image of topological insulator laser array when all peripheral sites are pumped at the same level. **c** Spectral evolution of the laser emission as a function of the peak pump current. **d** Measured light-current curve of the laser. The resolution of the spectrometer is 0.2 nm.

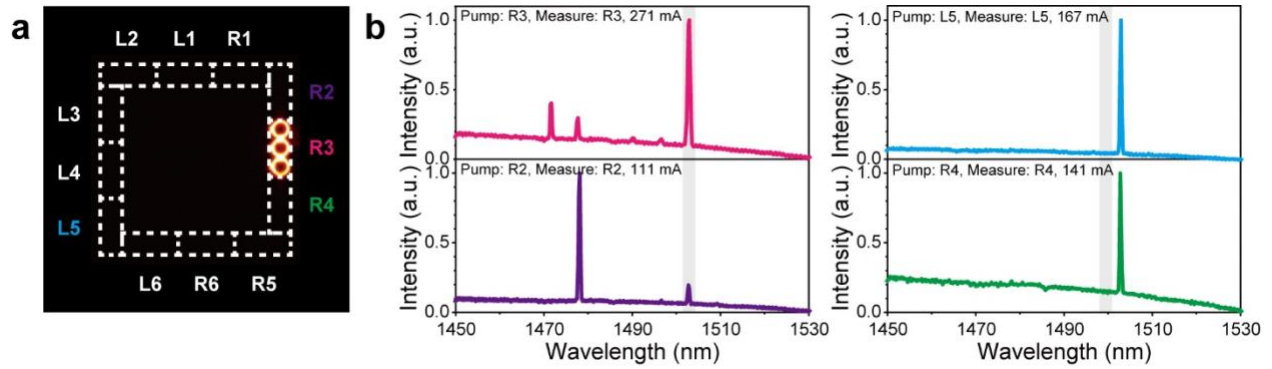


Figure 4 | Topological edge mode vs. locally excited modes. **a** Profile intensity image when the current is injected into only one of the twelve electrodes (in this case R3). **b** Measured electroluminescent spectra when the current is injected into different electrodes. The topological edge mode at a wavelength of 1503 nm persists in all cases (grey shaded area) while in some cases localised modes are excited that prevail the spectrum.

Supplementary Information for

Room temperature electrically pumped topological insulator lasers

Jae-Hyuck Choi¹, William E. Hayenga^{1,2}, Yuzhou G. N. Liu¹, Midya Parto², Babak Bahari¹,

Demetrios Christodoulides², and Mercedeh Khajavikhan^{1,2*}

¹Ming Hsieh Department of Electrical and Computer Engineering, University of Southern California, Los Angeles, California 90089, USA.

²CREOL, The College of Optics & Photonics, University of Central Florida, Orlando, Florida 32816–2700, USA.

*email: khajavik@usc.edu

Note 1. Wafer structure and fabrications procedure

The electrically pumped topological insulator laser is based on an InGaAsP/InP epitaxial structure, grown on an undoped InP substrate by molecular beam epitaxy (MBE) (Table S1). The gain region consists of 320 nm of undoped multiple quantum wells, sandwiched between an n -doped (with a thickness of 550 nm) and a p -doped (with a thickness of 700 nm) InP layers. The multiple quantum well structure is comprised of 10 layers of $\text{In}_{x=0.564}\text{Ga}_{1-x}\text{As}_{y=0.933}\text{P}_{1-y}$ (each with a thickness of 10 nm) placed between 11 layers of $\text{In}_{x=0.737}\text{Ga}_{1-x}\text{As}_{y=0.569}\text{P}_{1-y}$ (each with a thickness of 20 nm). Highly doped n -InGaAs and p -InGaAsP layers form the n - and p -contacts, respectively. The doping levels in the p - and n -doped InP layers, in the upper and lower sides of the gain region, gradually increase to reach the highest level at the contact layers. The epitaxial structure, designed by our group, was grown by OEpic Semiconductors Inc. [1].

Material	Loop	Thickness (nm)	Dopant	Comment
InGaAs	1	125	Zn ($p \sim 2E19 \text{ cm}^{-3}$)	n -contact layer
p -InP	1	350	Zn ($p \sim 5E18 \text{ cm}^{-3}$)	Cladding
p -InP	1	350	Zn ($p \sim 1E18 \text{ cm}^{-3}$)	
$\text{In}_{x=0.737}\text{Ga}_{1-x}\text{As}_{y=0.569}\text{P}_{1-y}$	1	20	Undoped	QW barriers
$\text{In}_{x=0.564}\text{Ga}_{1-x}\text{As}_{y=0.933}\text{P}_{1-y}$	10	10	Undoped	QWs
$\text{In}_{x=0.737}\text{Ga}_{1-x}\text{As}_{y=0.569}\text{P}_{1-y}$	10	20	Undoped	QW barriers
n -InP	1	300	Si ($n \sim 1E18 \text{ cm}^{-3}$)	Cladding
n -InP	1	250	Si ($n \sim 5E18 \text{ cm}^{-3}$)	
InGaAsP	1	125	Si ($n \sim 2E19 \text{ cm}^{-3}$)	p -contact layer
InP	1	1000	Si ($n \sim 2E19 \text{ cm}^{-3}$)	Buffer
InP substrate			Undoped	

Table S1. Detailed wafer structure with doping levels and layer thicknesses.

In order to fabricate the electrically pumped topological insulator lasers (Figure S2), first, the pattern of the structure is defined onto FOx-16 e-beam resist by high-resolution e-beam lithography (Fig. S2a), then it is transferred into the wafer by a reactive ion etching (RIE) process using $\text{H}_2:\text{CH}_4:\text{Ar}$ (10:40:7 sccm) plasma (Fig. S2b). Figure S3 presents the scanning electron microscope (SEM) image of the array at this stage of fabrication. Next, a 240 nm thick silicon nitride (Si_3N_4) film is deposited by plasma-enhanced chemical vapor deposition (PECVD) (Fig. S2c). To access the underlying highly doped InGaAsP layer, the cathode-electrode pattern is defined by photolithography, followed by a sequential dry etching of the Si_3N_4 layer, and wet etching of the remaining InP n -doped layer. Finally, the cathode-electrode is formed by photolithography and metal deposition of Ni/AuGe/Au (5/75/300 nm) (Fig. S2d). After photoresist liftoff, to planarize the surface before depositing the anode-electrode, the surface is spin-coated by an optically transparent polymer material (benzocyclobutene, BCB). Even though the BCB polymer is expected to provide a uniform planarization layer on the sample, in practice it tends to show some non-uniformities. The presence of these non-uniformities makes it difficult to properly pump the lasers, thus causing issues with overheating. In some cases, like on top of the gratings, we noticed that it is even more difficult to fully etch down the BCB and reach the contact layers for pumping. As a result, in our samples, the gratings remained fully unpumped. These issues may be addressed by developing new BCB spinning techniques and using thicker metal layers for electrodes. The thickness of the BCB layer was reduced by $\text{O}_2:\text{CF}_4$ (10:5 sccm) plasma etching until the top of the topological lattice structure is extruded (Fig. S2e). The anode-electrode area is then defined by photolithography. To reach the InGaAs p -contact layer, the additional Si_3N_4 layer and FOx-16 are removed from the top of the device using an RIE dry-etching process followed by a BOE wet-etching step (Fig. S2f). The anode-electrode metal film Ti/Au (15/300 nm) is then deposited using thermal evaporation (Fig. S2g). After liftoff, a rapid thermal

annealing (RTA) is performed at a temperature of 380 °C for 30 s to fuse the metal and reduce the resistance of the contact (Fig. S2h). Lastly, the sample is mounted on a header and is wire-bonded for optical and electrical characterizations (Fig. S2i).

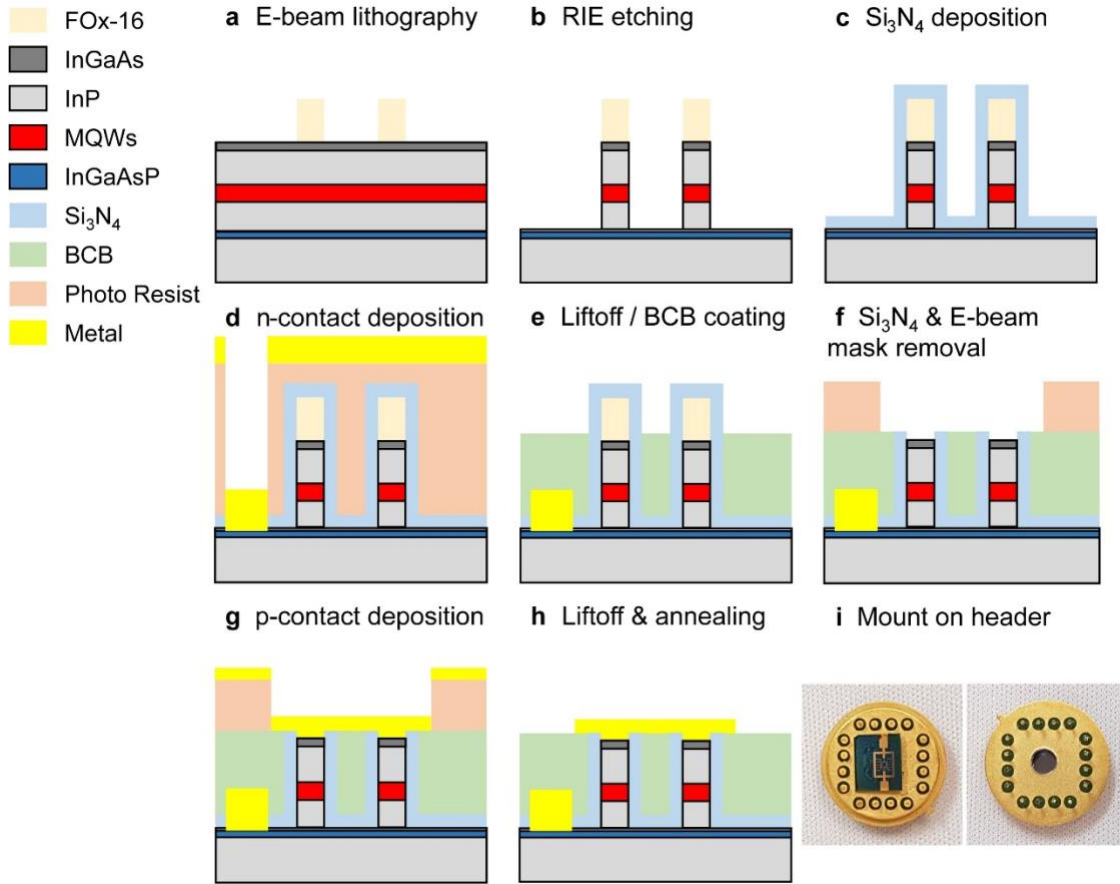


Figure S2. Fabrication steps involved in realizing electrically pumped topological insulator lasers. **a** The lattice structure is defined on a FOx-16 resist using e-beam lithography. **b** Pattern is transferred to the wafer using RIE etching. **c** Silicon Nitride is deposited using PECVD. **d** Cathode-electrode is fabricated on the InGaAsP contact layer. **e** After liftoff, BCB is spin-coated and dry etched. **f** The excess Silicon Nitride and FOx-16 are removed. **g** Anode-electrode is deposited on the InGaAs *p*-contact layer. **h** Liftoff and annealing are performed. **i** The sample is mounted on the header and wire-bonded to the pins.

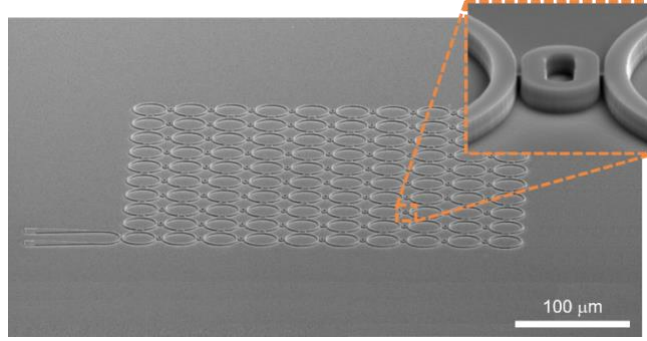


Figure S3. Scanning electron microscope (SEM) image of a fabricated topological insulator laser array. A 10×10 resonator network is connected via link structures. Inset: An image of a link resonator and its adjacent ring resonators. A 200 nm gap exists between the ring resonator and the off-resonant link. The etched depth of the structure is 1650 nm. The gain region can be identified in the middle of the structure.

Note 2. Electromagnetic simulations

In order to identify the lasing mode in the standalone ring resonators, finite element method (FEM) simulations are performed using COMSOL Multiphysics package. The microring resonator used in this simulation has a radius of $15 \mu\text{m}$ and a width of $1.4 \mu\text{m}$. The cross section of the microring is composed of InGaAsP multiple quantum wells sandwiched between InP cladding layers and the sidewall is covered by a 240 nm thick Si_3N_4 film. The structure is covered by BCB on the side and air on top. To find the eigenmodes in the microring resonators, a 2-D axisymmetric simulation is performed using eigenmode solver module (Fig. S4a). Here, the refractive index of the gain region (MQWs) is 3.4 [2] and the refractive index of InP is 3.14 [3]. Figure S4a shows the fundamental transverse electric mode (TE_0), primarily confined in the InGaAsP multiple quantum wells region. With this cross section profile, the effective index of the TE_0 mode is $n_{\text{eff}} = 3.2$. This effective index is used to perform the 2-D simulation of a ring resonator with a radius of $15 \mu\text{m}$ (Fig. S4b).

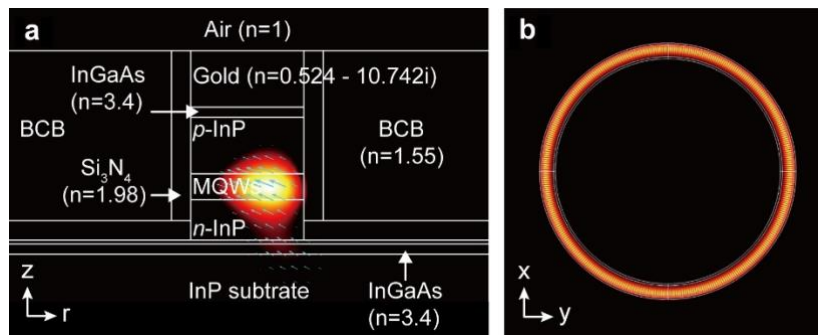


Figure S4. Lasing mode in a standalone ring resonator. **a** Cross section of the electric field intensity distribution shows the confined mode in the multiple quantum well gain region. The effective index of the mode is 3.2. **b** Electric field intensity distribution of the fundamental transverse electric (TE_0) mode inside the 2-D ring resonator.

Note 3. Measuring coupling strength

In our experiments, we characterize the coupling strength between two site ring resonators. The coupling is mediated by a link resonator [4]. To do this, we fabricate a basic building block of the structure, comprising of two site rings and one off-resonant link on the electrically pumped wafer as shown in Note 1. The gap size between the rings and link is 200 nm and the structural parameters of the elements are the same as the topological insulator laser reported in the main manuscript. Under optical pumping, a frequency splitting of ~ 31 GHz (0.245 nm in wavelength) is observed in the emission spectrum which indicates a coupling strength of $\kappa = \Delta\nu/2 = 15.5$ GHz.

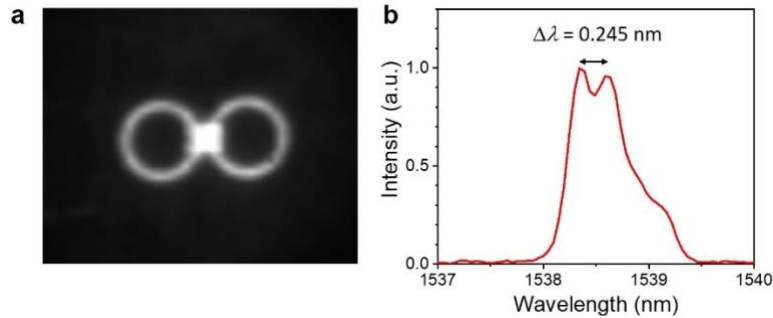


Figure S5. **a** The captured emission profile image from two ring resonators coupled via a link resonator when all the elements are optically pumped. **b** The spectrum shows a frequency splitting of 0.245 nm corresponding to a coupling strength of 15.5 GHz.

Note 4. Characterization setup

Figure S6 depicts the schematic of a dual function measurement station, designed for simultaneous micro-electroluminescence (μ -EL) and micro-photoluminescence (μ -PL) characterizations. For μ -EL characterization, the samples are examined under pulsed pumping, using a current driver (ILS Lightwave LDP-3840B) with a pulse width of 300 ns (100 ns) and a period of 50 μ s when all (one) anode electrodes are connected. A 10 \times microscope objective lens with a numerical aperture of 0.26 is used to collect the emission from the topological insulator lasers. The surface of the sample is imaged by two cascaded 4- f imaging systems into a NIR camera (Xenics Inc.). A broadband ASE source that passes through a rotating ground diffusing glass is used to illuminate the sample surface (as an incoherent source). A notch filter is placed in the path of emission to attenuate the pump beam. The emission spectra are obtained using a spectrometer (Princeton Instruments Acton SP2300) with an attached linear array detector (Princeton Instruments OMA V).

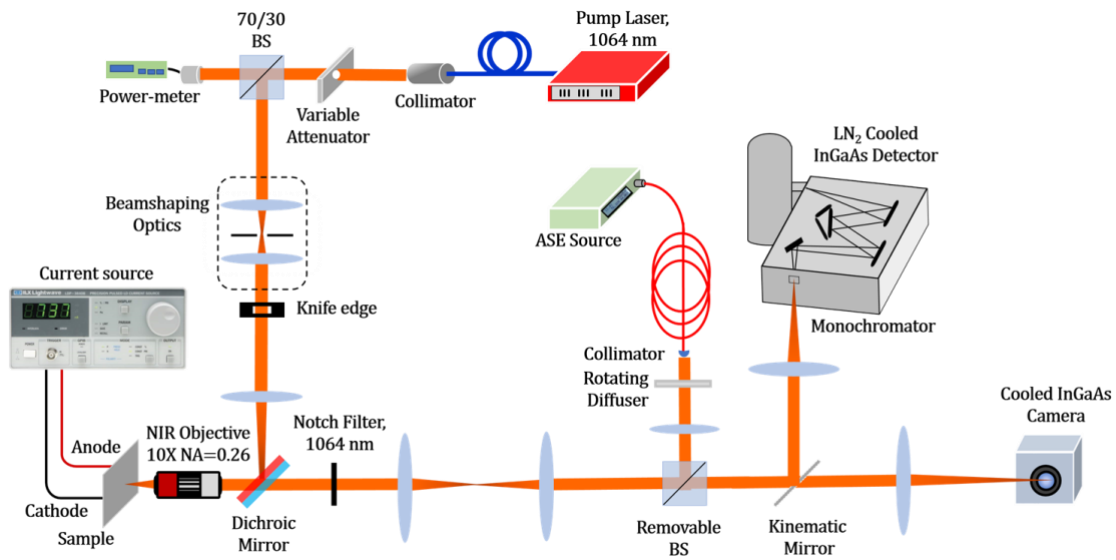


Figure S6. Schematic of the micro-electroluminescence and micro-photoluminescence characterization setup. The topological insulator laser is pumped by a pulsed current source. The emission is collected by a $10\times$ objective lens and directed into an NIR detector array for spectral measurements or to a NIR camera for intensity profile observation.

The μ -PL characterization part of the setup is utilized to examine the existence of the topological edge modes under optical pumping condition. In this setup a pump laser (SPI fiber laser) beam at a wavelength of 1064 nm is used with a duration of 15 ns and duty cycle of 0.4% (Fig. S6). The $10\times$ microscope objective is used to project the pump beam on the ring resonator and also serves to collect the emission. A square-shaped metallic intensity mask and a knife edge are placed at the object plane of the imaging system. The shadow of the metal mask and the knife edge are imaged on the sample surface to provide the desired pump profile as shown in Fig. S7.

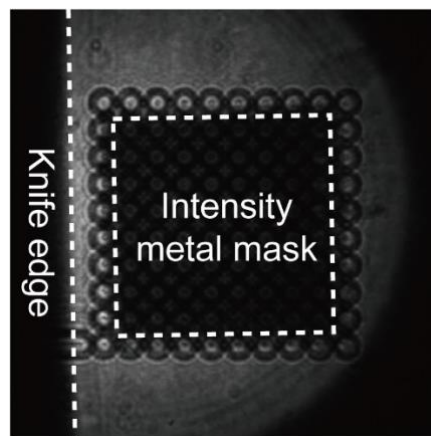


Figure S7. Optical pump profile provides gain along the perimeter of the array to promote the lasing of the topological edge mode.

Note 5. Measured lasing spectra from electrically pumped topological insulator laser at various edge elements

Figure S8 shows the collected emission from sites L2, L4, L5 and R6 when all the perimeter elements are electrically pumped. In all these cases, the lasing peak was observed at a wavelength of 1503 nm (similar to what was measured at R3). Also, as can be seen in these plots, the spectra all around the cavity exhibit single mode lasing behavior.

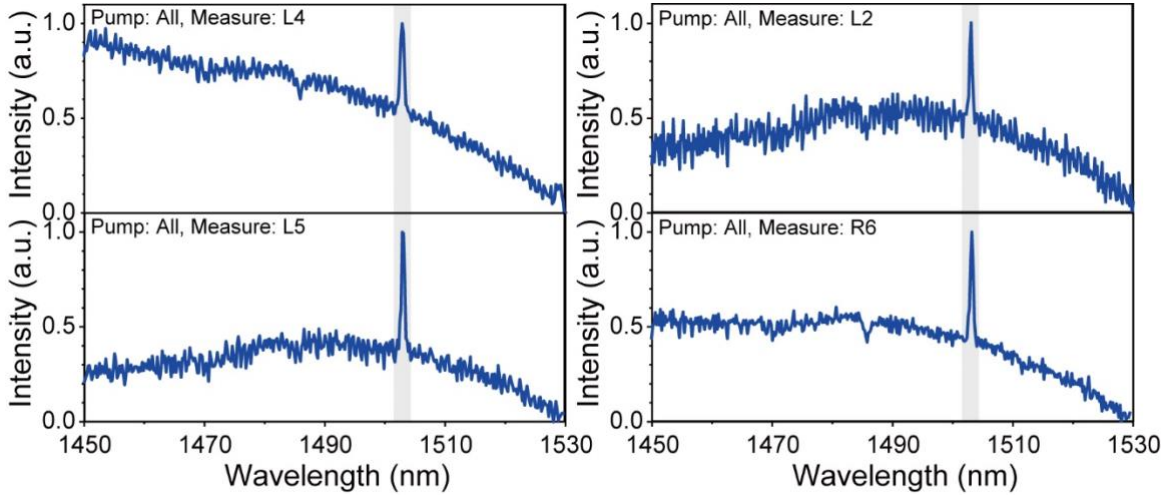


Figure S8. Measured emission spectra under electrical pumping at various sites (L2, L4, L5, and R6).

Note 6. Measured I-V curves of topological insulator laser

Figure S9 shows I-V curves of a topological insulator laser when all the electrodes are connected (Figure S9a), and only one electrode is connected (Figure S9b).

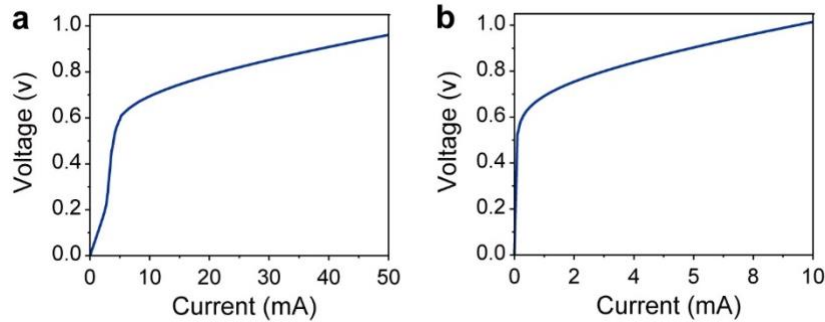


Figure S9. Measured I-V curves from topological insulator lasers when **a** all the electrodes are connected, and **b** only one electrode is connected.

Note 7. Comparison of topologically trivial and non-trivial lattices

To compare the lasing properties of the topologically trivial and non-trivial lattices, we characterize a topologically trivial lattice that has no position shift of the link resonators ($\Delta x = 0$). This corresponds to the $\alpha = 0$ case. Unlike the emission spectra collected from the topological insulator laser array, when the perimeter of the trivial lattice is pumped, multiple longitudinal lasing modes appear in the spectrum. Figure S10 compares the lasing spectra of topologically trivial and non-trivial lasers when the perimeters of the arrays are pumped at the same level. Please notice that for demonstration purposes the spectrum of trivial lattice is scaled up by a factor of 3.

The measurements are performed on samples of electrically pumped devices before the deposition of the electrodes. After depositing the metal electrodes, the trivial lattice shows no lasing, whereas the topological array lased as shown before.

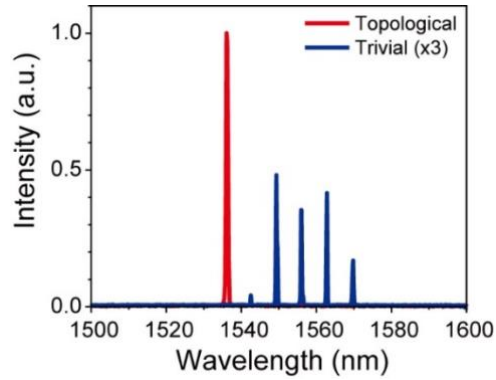


Figure S10. Measured emission spectra of topologically trivial and non-trivial laser arrays under the same pump level.

Note 8. Robustness of topological insulator laser to disorder

In order to investigate the robustness properties of the topological insulator lasers to disorder, we examine a topological insulator structure with missing site rings (un-pumped) on the perimeter elements (Fig. S11). When all the perimeter elements of the array are electrically pumped via the twelve electrodes, a single mode lasing peak is observed from different pumping sites. This result shows that our electrically pumped topological insulator lasers exhibit topological protection even if some of site rings are not pumped or missed.

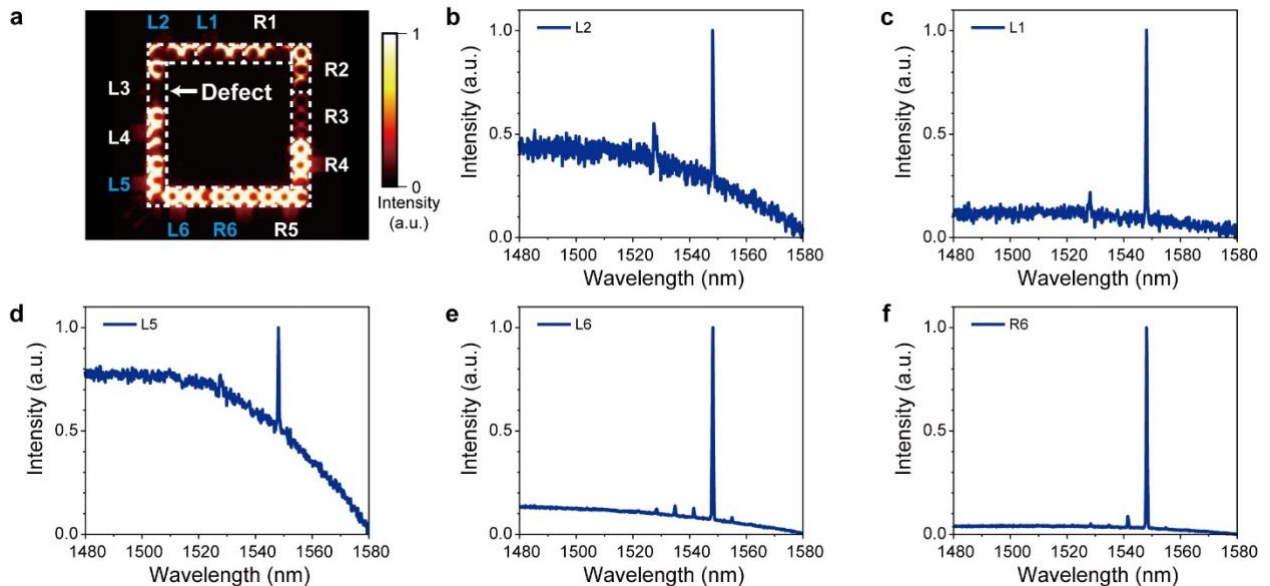


Figure S11. **a** Intensity profile images of topological insulator laser when two site rings of the topological edge element are not electrically pumped. **b-f** Measured electroluminescent spectra at each different site.

Note 9. Coherence measurement

To confirm that our topological laser elements emit in a coherent fashion, the interference patterns formed by the emission from various sites along the periphery of the array are measured. In order to perform this measurement, we modified our measurement setup by adding two branches operating as a Mach-Zehnder interferometer. Figure S12 shows a schematic diagram of this modified setup. Each interferometer arm has a moving iris that can select the emission from a desired site. These emissions are overlapped and the resulting interference fringes are imaged in the camera. Figure S13a shows the measured interference images obtained by overlapping emission from two neighboring sites when the perimeter of the topological insulator laser is electrically pumped. On the other hand, Fig. S13b depicts the interference result from two neighboring elements in the trivial laser under optical pumping- where no fringes could be identified. Unfortunately, interference measurements between larger apart sites were not performed due to the limitation of the field of view in our setup. In order to verify the extension of the coherence across the topological laser array, we repeated the interference measurement for every two consecutive elements on the edge (1&2, 2&3, 3&4, etc.). Figure S14 shows the resulting fringes of this extensive study along one edge. These measurements together with the observed single mode lasing operation can be an indication of a widespread coherence over the entire edge elements in the topological laser array.

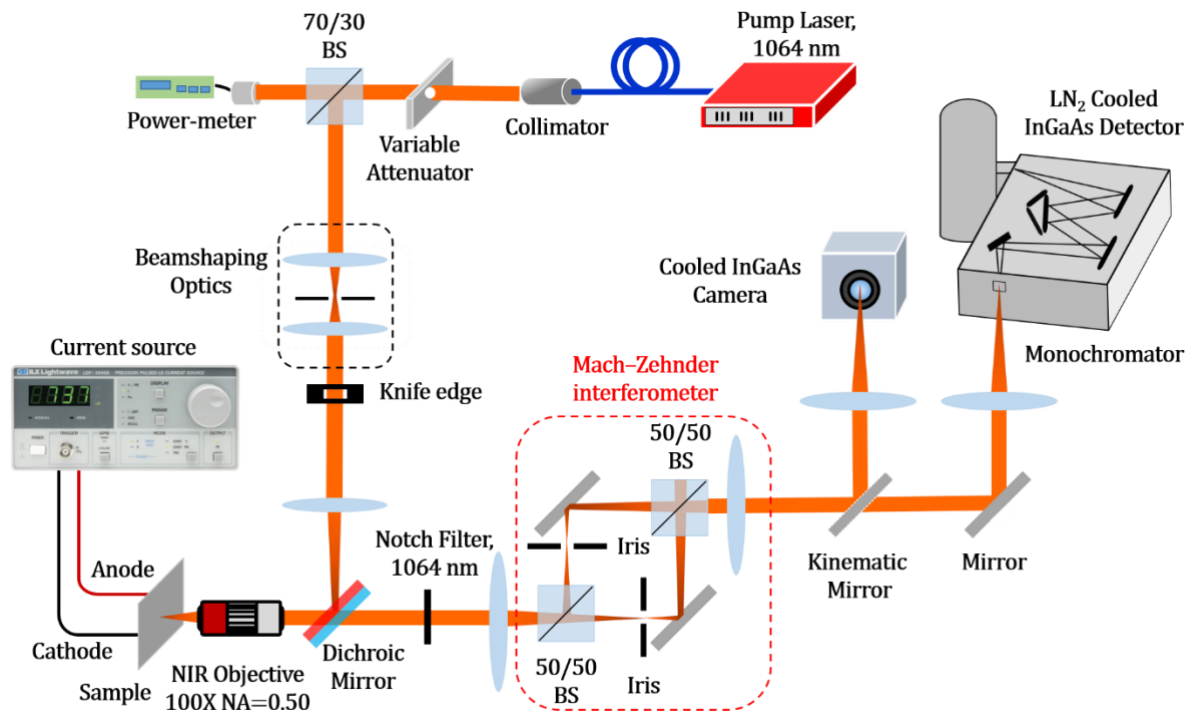


Figure S12. Schematic of the micro-electroluminescence characterization setup with the added Mach-Zehnder interferometer for measuring coherence.

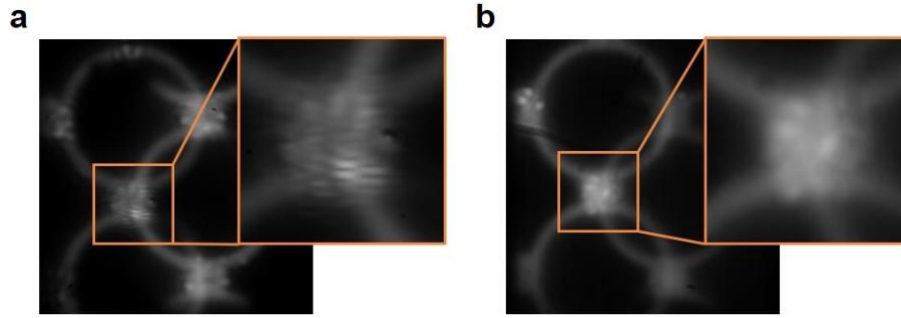


Figure S13. Measured intensity profile of interference fringes when the emission of two different neighboring site rings of the **a** topologically non-trivial and **b** trivial arrays are overlapped. Inset: Magnified interference pattern image. The topological laser shows interference fringes, while no such fringes could be observed in the trivial laser array.

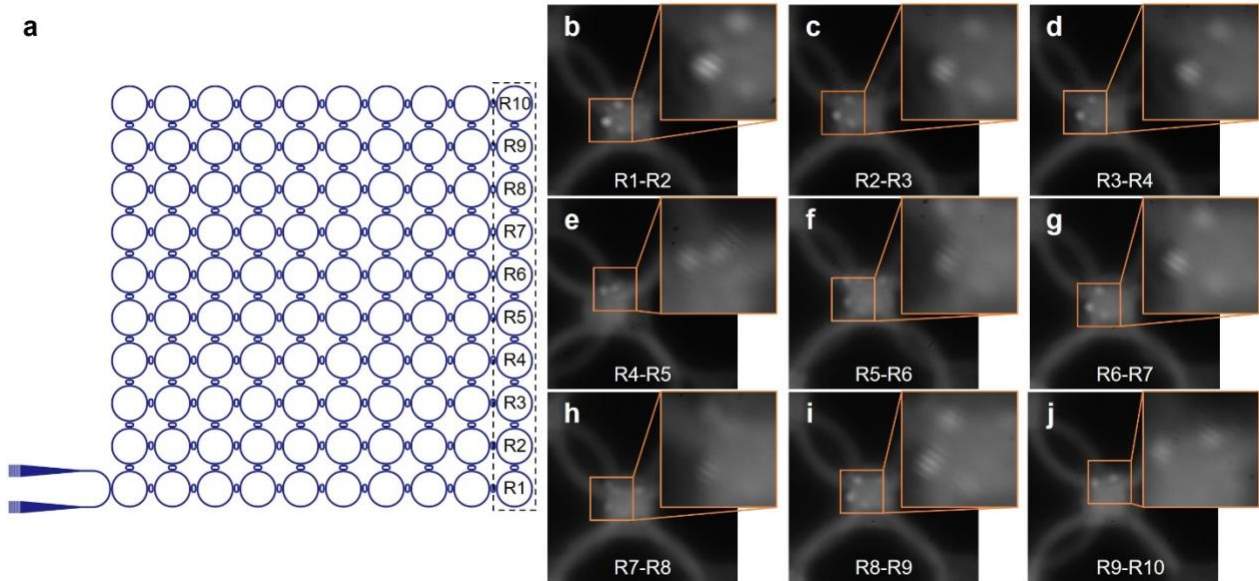


Figure S14. a A schematic diagram of the topological laser array showing the location of the overlapped ring elements. **b-j** Measured interference fringes for elements along one edge of the topological laser array. Insets: Magnified interference pattern image.

Note 10. Unidirectional lasing by incorporating S-bends inside the site ring resonators

We should note that our current structure is not designed to lase in a predetermined unidirectional fashion. In quantum spin Hall based topological lasers, pumping can excite both clockwise (CW) and counter clockwise (CCW) modes. While no unidirectionality is expected from passive quantum spin Hall photonic arrangements, the lasers based on this effect tend to show some degree of chirality because of the hole burning mechanism in inhomogeneously broadened gain systems. However, since we did not collect the emission from the gratings, we cannot verify if and to what extent the emission is unidirectional. Nevertheless, spontaneous breaking of chirality offers no practical advantage in lasers.

We are currently working on adding S-bends to our electrically pumped topological lasers to enforce predetermined unidirectionality in our lasers. However, adding these constructs, even though possible, requires overcoming several additional challenges. For example, the distance between the S-bends and the rings must be precisely controlled. Also, due to the larger width of the waveguides, the tapering of S-bends becomes more difficult. Finally, one should expect much more non-uniformities of BCB layer in the rings with S-bends, thus causing issues with good quality electrodes.

We designed the electrically pumped lasers with S-bends as shown in Fig. S15, and characterized the laser performance under optical pumping (without depositing the electrode). From the strong emission emerging from one of the grating output couplers, we can confirm that the S-bend design leads to unidirectional operation. As mentioned above, fabricating uniform top electrodes for both rings and S-bends is quite challenging. We are currently working to find a solution for this problem for our future designs.

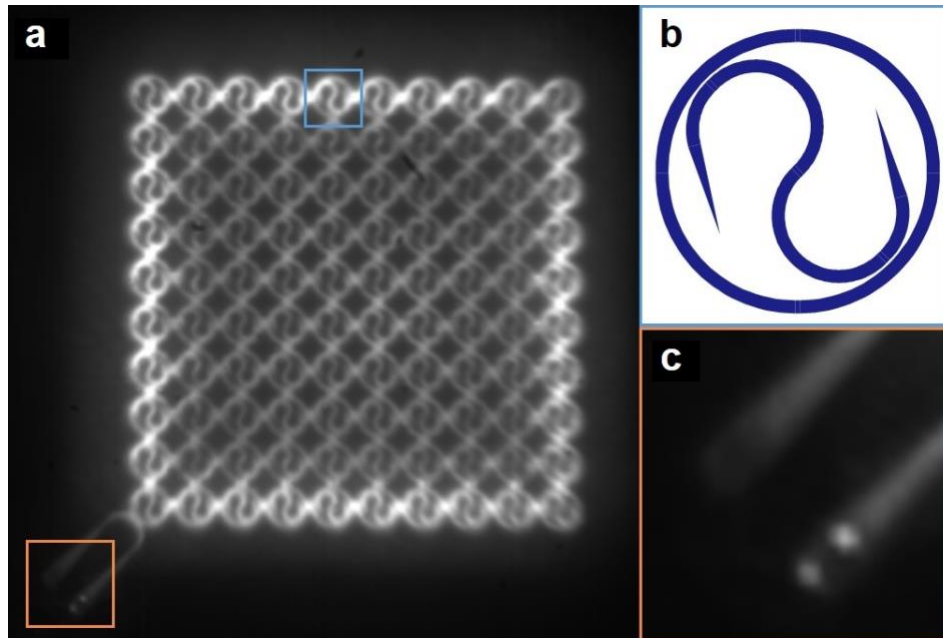


Figure S15. **a** Measured intensity profile from a topological insulator array fabricated on a wafer suitable for electrical pumping with S-bends inside the ring resonators. The measurement is performed through optical pumping and prior to top electrode deposition. **b** A ring resonator with an S-bend. **c** The magnified image of the grating output couplers. The unidirectionality of the topological edge mode can be confirmed from the strong emission observed at only one of the grating couplers.

Supplementary References:

1. Hodaei, H. et al. Parity-time-symmetric microring lasers. *Science* **346**, 975–978 (2014).
 2. Khajavikhan, M. et al. Thresholdless nanoscale coaxial lasers. *Nature* **482**, 204–207 (2012).
 3. Adachi, S. Optical dispersion relations for GaP, GaAs, GaSb, InP, InAs, InSb, $\text{Al}_x\text{Ga}_{1-x}\text{As}$, and $\text{In}_{1-x}\text{Ga}_x\text{As}_y\text{P}_{1-y}$. *Journal of Applied Physics* **66**, 6030-6040 (1989).
- Bandres, M. A. et al. Topological insulator laser: experiments. *S*